



Surface velocity of the Northeast Greenland Ice Stream (NEGIS): Assessment of interior velocities derived from satellite data by GPS

Christine S. Hvidberg¹, Aslak Grinsted¹, Dorthe Dahl-Jensen¹, Shfaqat Abbas Khan², Anders Kusk²,
Jonas Kvist Andersen², Niklas Neckel³, Anne Solgaard⁴, Nanna B. Karlsson⁴, Helle Astrid Kjær¹, Paul
5 Vallelonga¹.

¹Niels Bohr Institute, University of Copenhagen, Copenhagen, Denmark.

²DTU-Space, Technical University of Denmark, Kgs. Lyngby, Denmark.

³Alfred-Wegener-Institut, Helmholtz-Zentrum für Polar- und Meeresforschung, Bremerhaven, Germany.

⁴Geological Survey of Denmark and Greenland, Copenhagen, Denmark.

10

Correspondence to: Christine S. Hvidberg (ch@nbi.ku.dk)

Abstract. The Northeast Greenland Ice Stream (NEGIS) extends around 600 km upstream from the coast to its onset near the ice divide in interior Greenland. Several maps of surface velocity and topography in the interior Greenland exist, but the accuracy is not well constrained by in situ observations and limiting detailed studies of flow structures and shear margins near 15 the onset of NEGIS. Here we present the results from a GPS mapping of surface velocity in an area located approximately 150 km from the ice divide near the East Greenland Ice-core Project (EastGRIP) deep drilling site (75°38' N, 35°60' W). A GPS strain net consisting of 63 poles was established and observed over the years 2015-2019. The strain net covers 35 km along NEGIS and 40 km across NEGIS, including both shear margins. The ice flows with a uniform surface speed of approximately 55 m a⁻¹ within a >10 km wide central flow band with strain rates in the order of 10⁻⁴ a⁻¹. The strain rates increase in the shear 20 margins by an order of magnitude, and 10-20 m deep shear margin troughs mark a zone with enhanced longitudinal stretching, transverse compression and shear. We compare the GPS results to the Arctic Digital Elevation Model (ArcticDEM) and a list of satellite-based surface velocity products in order to evaluate these products. For each velocity product, we determine the bias and precision of the velocity compared to the GPS observations, as well as the smoothing of the velocity products needed to obtain optimal precision. The best products have a bias and a precision of ~0.5 m a⁻¹. We combine the GPS results with 25 satellite-based products and show that organized patterns in flow and topography emerge in the NEGIS ice stream when the surface velocity exceeds approximately 55 m a⁻¹ and are related to bedrock topography.

1 Introduction

The discharge from Greenland's marine terminating outlet glaciers has increased over the last decades and contributed to the increasing mass loss from the Greenland ice sheet (Mouginot et al., 2019; Mankoff et al. 2019; Imbie Team, 2019). During the 30 same period, many outlet glaciers have accelerated and thinned in response to changes in atmospheric and oceanic forcings, thereby adding to the dynamic mass loss (Bevis et al. 2019; Khan et al., 2015). Further dynamic thinning and acceleration in



ice flow at marine outlet glaciers can potentially propagate inland, and activate the vast high-elevation and slow moving interior part of the ice sheet, thereby leading to additional mass loss (Mouginot et al., 2019).

Fast flowing ice streams drain a significant fraction of the ice from the Greenland Ice Sheet into marine outlet glaciers and
35 they thereby connect the interior parts of the ice sheet with the margins. The fast flow involves basal sliding and friction at the bed and along the shear margins, but the understanding of the mechanisms controlling ice stream dynamics and their connection to the surrounding slow-moving ice is incomplete (Minchew et al., 2019; Minchew et al., 2018; Stearns and van der Veen, 2018, Gillet-Chaulet et al. 2016). In the interior, in situ observations of surface movement are sparse and limited to a few locations (e.g. Hvidberg et al. 1997; Hvidberg et al. 2003), and satellite-based observations of surface velocity and elevation
40 change are limited by their temporal and spatial resolution and the lack of validation data (Joughin et al., 2017). As a result, there is a significant uncertainty in the projections of the future response of the interior areas of the Greenland Ice Sheet to changes at the marine outlet glaciers (Imbie Team, 2019; IPCC, 2019).

The North-East Greenland Ice Stream (NEGIS) drains a basin in northeast Greenland with an area of about 16% of the total area of the Greenland ice sheet into three main marine outlet glaciers, Nioghalvfjerdsfjorden glacier (NG), Zachariae Isstrøm
45 (ZI), and Storstrømmen Glacier (SG) (Fig. 1). NEGIS extends around 600 km upstream of its outlet glaciers to its onset near the ice divide in the interior of northern Greenland. The inferred mass loss from NEGIS has increased since after 2003 (Mouginot et al. 2019). This is mainly due to a rapid retreat of ZI since it lost its floating tongue in 2003 and a slow retreat of NG (Khan et al. 2014; Mouginot et al. 2015), while SG has slowed down after its surge around 1980 (Mouginot et al. 2018). If the marginal loss continues and induce dynamical thinning and acceleration upstream along NEGIS, it could potentially
50 activate the interior parts of NEGIS (Khan et al., 2014; Choi et al. 2017). The onset of NEGIS in the interior may be related to the geothermal heat flux and subglacial drainage system in the area (Karlsson and Dahl-Jensen, 2015), but the sensitivity of the system to the ongoing marginal mass loss is not well known.

Here, we present results from a geodetic surface program to characterize surface topography and ice flow of an interior section of NEGIS in an area near its onset in North Central Greenland, and to assess remote sensing products from this interior area
55 of the Greenland ice sheet. The area is located approximately 150 km from the ice stream onset near the East Greenland Ice-core Project (EastGRIP) deep drilling site (75°38' N, 35°60' W, 2700 meters above sea level). We compare our GPS derived heights and surface velocities with the ArcticDEM height model (Porter et al. 2018), as well as with 165 published and experimental remote sensing velocity products from the NASA MEaSUREs program, the ESA Climate Change Initiative, the PROMICE project, and three experimental products based on data from the ESA Sentinel-1, the DLR TerraSAR-X, and USGS
60 Landsat satellites, in order to validate and assess these products (see complete list and references in section 4 below). We use the GPS derived horizontal surface velocities and strain rates in combination with the remote sensing velocity products to characterize the ice stream flow, shear margins and structure of NEGIS near its onset.



2 GPS data and methods

2.1 GPS stake network

65 The surface program includes a repeated in situ survey using the Global Positioning System (GPS) with a strain net consisting of 63 stakes. Observations cover the years 2015-2019. The stake network was established in 2015 with 16 stakes near the EastGRIP deep drilling site ($75^{\circ}38' N$, $35^{\circ}60' W$, 2700 masl), and gradually expanded in 2016, 2017 and 2018 to include 63 stakes (Fig. 2). The growing network of stakes were measured by GPS every year from 2015 to 2019 and supplemented with additional temporary stakes that were measured only once. The layout of the stakes was designed to provide 1) transects of
70 flow velocities along and transverse to the flow, and 2) longitudinal and transverse strain rates in the center of the fast flow and at both shear margins. To fulfill these requirements, the stake network contains sets of stakes placed in a diamond shape centered around the mid-point of NEGIS and at both shear margins. The stake network extends 35 km along NEGIS and 40 km across NEGIS, thereby covering the entire 25 km width of NEGIS and extending across both shear margins into the slower moving regions outside the ice stream. The purpose of the additional stakes added in 2018 was to obtain detailed information
75 of strain rates across a topographic surface undulation northwest of the EastGRIP site (Fig. 2). All stake observations are included in this analysis.

The GPS observations were carried out with a Leica GX1230 GPS receiver with data acquisition lasting minimum 1 hour, and typically 2-4 hours. The GPS antenna was mounted on the top of each stake, and the height above the surface was measured manually. The stakes were 3.5 m long aluminum stakes; they were drilled approximately 2 m below the surface and extended
80 when needed due to a continuous snow accumulation in the area (approximately 0.3 m of snow equivalent per year; Vallelonga et al. 2014). All stakes established in 2015, 2016 and 2017 were extended during the observational period when the antenna heights decreased below 1 m above the surface. A few stakes were moved and/or replaced due to camp activities.

The GPS observations were post-field processed using the open source software package ESA/UPC GNSS-lab tool (gLAB) (Sanz Subirana et al. 2013; Ibáñez et al. 2018). We used the International GNSS Service (IGS) combined orbit/clock product,
85 we applied ionospheric corrections, we took the antenna phase center offset into account, and we used the software in static mode. An automated protocol was developed in order to perform a systematic Precise Point Positioning (PPP) processing of the stake observations from each year, including multiple observations of some of the stakes within the annual field seasons. The gLAB processing protocol was assessed by comparing processing results from two one-hour observations with PPP processing results from the GIPSY-OASIS version 6.4 software developed at the Jet Propulsion Laboratory (JPL). We use JPL
90 final orbit products, which include satellite orbits, satellite clock parameters and Earth orientation parameters. The orbit products take the satellite antenna phase center offsets into account. Receiver clock parameters are modeled, and the atmospheric delay parameters are modeled using the Vienna Mapping Function 1 with VMF1 grid nominal (<http://vmf.geo.tuwien.ac.at/>) (Kouba, 2007; Boehm et al, 2006). Corrections are applied to remove the solid Earth tide and ocean tidal loading. The amplitudes and phases of the main ocean tidal loading terms are calculated using the Automatic
95 Loading Provider (<http://www.oso.chalmers.se/~loading>) (Scherneck and Bos, 2002) applied to the FES2014 ocean tide model



including correction for center of mass motion of the Earth due to the ocean tides. The site coordinates are computed in the IGS14 frame (Altamimi et al, 2016). All GIPSY-OASIS processing results were within <1.7 cm of the gLAB processing results (see Table 1). We note this value as our processing uncertainty.

2.2 GPS velocities and surface elevations

100 To derive the horizontal surface velocity, a linear fit was performed to the observed Northing and Easting positions, respectively (projected to the National Snow and Ice Data Center (NSIDC) Sea Ice Polar Stereographic North and referenced to WGS84 horizontal datum (EPSG:3413)). A possible small tilt of the stake can lead to uncertainties in the horizontal position. We take this into account by including an unknown horizontal shift in the position of stakes that were vertically extended. For each stake, the shift was determined independently from the other stakes, and the linear fit and the shift were determined 105 simultaneously. The estimated shifts are in the range 0.05 m to 0.2 m, and often exceeds 0.10 m. The surface velocity was calculated by assuming that the flow is along the surface, thereby neglecting vertical movement. We estimate the uncertainty of the derived velocities due to the combined uncertainty of the GPS observations and the method to be in the order of 10^{-2} m a^{-1} . As a horizontal reference position of the stakes, we use the estimated horizontal position of the stakes on 2017-01-01, assuming a constant horizontal displacement of each stake over the observational period. We select a common reference for 110 the network in order to consistently derive horizontal strain rates and assess surface elevations, but the reference date is not an accurate timestamp due to the different initial dates of the stakes.

We also estimate a mean GPS derived surface elevation of the stakes to be used below for the assessment of satellite based observations. In the interior areas of the Greenland ice sheet, climate driven variations in snow accumulation and firn compaction lead to seasonal and interannual variations of the surface elevation that are not resolved by our annual GPS 115 observations. We estimate the mean GPS derived surface elevation as the mean of the individual observations at each stake, neglecting trends over the observational period due changes in snow accumulation, firn processes or ice dynamical changes. The resulting horizontal stake velocities are shown in Fig. 2, and the reference positions and horizontal velocities are listed in supplementary Table S1. The GPS derived surface elevations and the magnitudes of the horizontal stake velocities, are shown along three transects across NEGIS (see Fig. 3) and one transect along NEGIS (see Fig. 4). The stake velocities show that the 120 surface speed is relatively constant at approximately 56.6 m a^{-1} along the centerline of NEGIS, and is above 55 m a^{-1} in a >10 km wide central flow band. The GPS derived surface elevations reveal 20 meter deep topographic troughs at the shear margins. The direction of the fast flow at the center line is 33.5° from North.

2.3 GPS strain rates

125 After having derived horizontal surface velocities, we calculate horizontal strain rates, which are essential in understanding the ice flow pattern and internal stratigraphy of the ice stream and its surroundings. We calculate the horizontal principal strain rates in 32 different triangular sections within the GPS strain net. Each triangle is defined by a combination of three GPS stakes and assumes a linear velocity within the triangle, i.e. constant strain rates within the triangles (see Fig. 5). The principal strain



rates are generally in the order of 10^{-4} a^{-1} in a >10 km wide central flow band along NEGIS, as well as in the slow moving areas outside NEGIS. In the two shear margins, horizontal principal strain rates increase by an order of magnitude and reach 130 a maximum in the northern shear margin of $3.8 \cdot 10^{-3}$ a^{-1} (extension) and $-3.6 \cdot 10^{-3}$ a^{-1} (compression), and in the southern shear margin of $3.6 \cdot 10^{-3}$ a^{-1} (extension) and $-4.3 \cdot 10^{-3}$ a^{-1} (compression). In both shear margins, the principal strain rates are orientated in an angle of approximately $\pm 35^\circ$ relative to the direction of the flow, due to a combination of longitudinal extension, transverse compression and a high shear strain rate along the shear margins. The principal strain rates are slightly higher in the triangles north of the central flow line of NEGIS than in those south of the central flow line, probably because the northern 135 shear margin is wider than the southern shear margin and not captured as precisely by the GPS strain net as the southern shear margin. We estimate the uncertainty of the strain rates averaged over the triangles (>2 km) to be in the order of 10^{-5} a^{-1} .
Along a transect across NEGIS, we calculate the horizontal strain rate tensor along the direction of the flow at three stakes. The three stakes are located in the northern shear margin, in the center (EastGRIP site), and in the southern shear margin, respectively (Fig. 5). The strain rates along the direction of the flow are calculated as the mean of the rotated strain rate tensors 140 in the four adjacent triangles, and they are ± 2 km horizontal averages, corresponding to the dimensions of the adjacent triangles. The normal strain rate components along the direction of the flow at these three stakes are plotted in Fig. 3b. At the central flow line at the EastGRIP site, the normal strain rates are $(0.9 \pm 0.2) \cdot 10^{-4}$ a^{-1} in the longitudinal (along flow) direction, and $(-0.9 \pm 0.5) \cdot 10^{-4}$ a^{-1} in the transverse direction. The ± 2 km-average longitudinal and transverse strain rates relative to the local flow direction in the northern shear margin are $(0.8 \pm 1.9) \cdot 10^{-3}$ a^{-1} and $(-0.8 \pm 0.4) \cdot 10^{-3}$ a^{-1} , respectively. The horizontal 145 shear is $(-2.1 \pm 0.9) \cdot 10^{-3}$ a^{-1} . The ± 2 km-average longitudinal and transverse strain rates relative to the local flow direction in the southern shear margin are $(0.8 \pm 1.6) \cdot 10^{-3}$ a^{-1} and $(-1.3 \pm 0.5) \cdot 10^{-3}$ a^{-1} , respectively, and the horizontal shear is $(2.6 \pm 0.8) \cdot 10^{-3}$ a^{-1} . The resolution of the GPS strain net is limited by the position of the stakes and may not capture the peak strain rates at the shear margins, but the sharp transition in the southern shear margin stand out in the relative velocity pattern in Fig. S1 and in the strain rates along the transect across NEGIS (Fig. 3b).

150 **4 Comparison with satellite observations**

4.1 Comparison with a digital elevation model observed from space

The GPS derived surface elevations are used to validate the accuracy of the ArcticDEM release 7. The ArcticDEM is a digital elevation model (DEM) based on stereo auto-correlation techniques on visual imagery from Worldview satellites (Porter et al., 2018). The timestamp of the ArcticDEM in the EastGRIP area is 2017 (estimated), and the vertical accuracy has not been 155 verified (Porter et al., 2018), thus overlapped by the GPS observation period. We compare GPS derived surface elevations with the surface elevation sampled from the ArcticDEM at the stake positions (WGS84 ellipsoidal heights) and find an agreement within ± 1 m, except for one stake with a deviation of >1.5 m (Supplementary Fig. S2 and S3). Minor differences between the two datasets could be due to variable snow accumulation through the years, leading to seasonal and interannual



variability in surface elevation, which is captured differently by the two datasets due to their different timestamps. The outlier
160 is located in the exceptionally deep and narrow trough in the southern shear margin (Fig 3a). Local topography effects at these stakes could possibly be due to interpolation or shadow effects in the Arctic DEM (Porter et al., 2018). The mean difference between the 63 GPS derived surface elevations and the ArcticDEM at the location of the GPS stakes is 0.48 m with a standard deviation of 0.53 m, confirming the low uncertainty of the ArcticDEM (Noh and Howat, 2015; Porter et al., 2018).

4.2 Comparison with surface velocity products observed from space

165 The GPS derived surface velocities are used to validate and assess the accuracy of several available ice velocity products derived from satellite data from the interior of the Greenland ice sheet. The ice velocity can be derived from space using data from synthetic aperture radar (SAR) or optical sensors. Optical feature tracking can provide velocities in very high resolution from coherent pairs of visual images. In the interior of the Greenland ice sheet, the surface is mostly featureless and SAR processing methods between pairs of SAR images are useful to derive surface velocities, either based on speckle tracking or 170 on phase displacements from interferometric synthetic aperture radar (InSAR).

We include several experimental ice velocity products in our assessment, as well as several one-year and multi-year products constructed from various remote sensing sources and methods. For each type of velocity product, we have also calculated a long-term average of all the velocity maps, and included this in our assessment. In total, we include 165 velocity products from the following sources:

175 1) NASA MEaSUREs Multi-year Greenland Ice Sheet velocity map v1, 1995-2015 (Joughin et al., 2017) (MEaSUREs multi-year v1). This map was derived from InSAR, SAR, and Landsat 8 optical imagery data using a combination of speckle-tracking, InSAR and optical feature tracking methods, supplemented with balance velocities near the ice divides where the flow speeds are <5 m a^{-1} . The data are provided with a resolution of 250 m. In the interior of the ice sheet, the estimated errors of this product are up to ~ 2 m a^{-1} , and reported to be <1 m a^{-1} in areas where InSAR is used.

180 2) NASA MEaSUREs Greenland Ice Sheet winter velocity maps (September-May) from InSAR data v2, 2000-2018 (Joughin et al., 2010, 2018) (MEaSUREs InSAR v2). These maps were derived entirely from data obtained by CSA RADARSAT-1, JAXA ALOS, and DLR TerraSAR-X/TanDEM-X (TSX/TDX) satellites, as well as from ESAs C-band SAR data from Copernicus S-1A/B. The maps were produced using an integrated set of SAR, speckle-tracking and interferometric algorithms (Joughin, 2002). The data are provided with a resolution of 200 m and the error is estimated to be <10 m a^{-1} .

185 3) NASA MEaSUREs Greenland Annual and Quarterly Ice Sheet velocity maps from SAR and Landsat v1, 2015-2018 (Joughin et al., 2018) (MEaSURE SAR&Landsat v1). These maps are derived from SAR data obtained by DLR TerraSAR-X/TanDEM-X (TSX/TDX) and ESA Copernicus S-1A/B satellites, and from the USGS Landsat 8 optical imagery using a combination of speckle-tracking, InSAR and optical feature tracking methods (Joughin et al. 2018). The resolution of the data are 200 m.

4) ESA Climate Change Initiative (ESA CCI) Greenland Ice Sheet annual velocity maps by ENVEO, 2014-2018 from SAR

190 (ESA Greenland Ice Sheet CCI project team, 2018). These maps are derived from ESA Copernicus Sentinel-1A/B SAR data using feature tracking techniques. The resolution is 500m, and the estimated error is ~ 15 m a^{-1} (Nagler et al., 2015).



5) PROMICE Greenland velocity maps, 2016-2019 from SAR (Solgaard and Kusk, 2019; available from www.promice.dk). These products are derived from ESA Copernicus S-1A/B SAR data using offset tracking [Strozzi et al., 2002] by employing the operational interferometric post processing chain (IPP) (Kusk et al., 2018; Dall et al., 2015). Each map is a mosaic

195 consisting of both 12-day and 6-day pairs within two Sentinel 1A cycles, and thus the temporal resolution of the product is 24 days. A new map is available every 12 days. The spatial resolution is 500 m, and the estimated error is 10-30 m a⁻¹.

6) DTU-Space experimental Sentinel-1A/B (S-1) Greenland ice sheet velocity product, from InSAR (DTU-Space-S1). This product is derived from SAR data acquired by ESA Copernicus Sentinel-1A/B satellites in the period from 2019-01-01 to 2019-01-18 from two ascending and three descending tracks. Eight 6-day pairs and five 12-day pairs were processed using the

200 in-house-developed Interferometric Post Processing chain (IPP) (Kusk et al., 2018). Interferograms were co-registered using the Tandem-X 90 m DEM and a multi-year average of the PROMICE 2016-2019 offset-tracking velocity maps (see above). The relative velocity field from each unwrapped interferogram was calibrated to absolute values using slow-moving (<0.05 m a⁻¹) ground control points extracted from the same velocity map used for coregistration, and 3D velocities were generated assuming surface parallel flow.

205 7) AWI experimental TerraSAR-X (TSX) Greenland velocity product, from InSAR (AWI-TSX). The velocity field was derived from SAR interferometry obtained by DLR TSX by combining data from ascending and descending satellite orbits following well-established methods (e.g. Joughin et al., 1998). Three interferograms were formed from descending satellite data acquired between 2016-09-07 and 2016-10-01 and another three from ascending satellite data acquired between 2017-10-24 and 2018-01-03. All interferograms have a temporal baseline of 11 days with perpendicular baselines varying between 25

210 and 180 m. Due to the latter a certain topography induced phase difference is present in the interferograms, which was removed with the help of the global DLR TanDEM-X DEM with a 30 m grid resolution. The topography corrected interferograms were unwrapped using GAMMA's minimum cost flow algorithm (Werner et al., 2002) and combined to 3D velocity maps assuming surface parallel ice flow. In order to set the relative velocity estimates to absolute values seed points were extracted from the MEaSUREs multi year dataset, and adjacent velocity fields where patched together using the average value in their overlapping

215 areas. The final product was gridded to 30 m spatial resolution.

8) MEaSURE's experimental Inter-Mission Time Series of Land Ice Velocity and Elevation (ITS_LIVE) velocity product version Beta V0 (Gardner et al., 2019) (MEaSUREs ITS_LIVE). Surface velocities are derived from image pairs of USGS Landsat 4, 5, 7, and 8 optical imagery using the auto-RIFT feature tracking processing chain described in Gardner et al. (2018). Here we derived a multi-year velocity product from 1985 to 2018, averaged from the annual products. In our observed area,

220 the data is mainly derived from Landsat 8, and we therefore also derive an average of the annual product from 2013 to 2018, covered by the Landsat 8 imagery. The final product was gridded to 120 m spatial resolution. The images suffers from x- and y- geolocation errors of 15 m, and to correct for these errors the velocity components are tied to a stable surface, either to zero at rock surfaces in margin areas or to the median reference velocity in slow-moving areas. In interior Greenland, the MEaSUREs Greenland Annual Ice Sheet Velocity Mosaic from SAR and Landsat version 1 velocity product is used as the

225 reference velocity (Joughin et al., 2010).



The assessment consists of an inter-comparison between the GPS derived velocities of the stakes from the period 2015-2019 and the interpolated surface velocity at the location of the stakes from the satellite-based velocity products. For each velocity product, we determine the accuracy (the bias) and precision (the standard deviation, i.e. the root mean square difference (RMS) 230 after removing the bias), between the GPS velocities and the satellite-derived velocities at the location of the stakes. In addition to the direct inter-comparison between the GPS velocities and the satellite-based velocities, we also investigate the variability of the satellite-based velocity products. In order to do so, we perform a spatial smoothing of the satellite-based velocity product with a running mean filter with a smoothing length, and we then vary the smoothing length in order to determine the optimum smoothing length (σ) that minimize the standard deviation (RMS) between the GPS observations and the velocity product. 235 The results of the inter-comparison for the top ten products (sorted according to the standard deviation) are listed in Table 2 (with a complete overview of all products in Table S2), and it is illustrated in Fig. 6. It is important to note that the different time stamps and temporal coverage Δt of the observations are not taken into account in the inter-comparison. In satellite-based velocity products with longer temporal coverage, possible temporal variability and/or noise are smoothed, and there is a clear relationship between increasing temporal coverage and decreasing bias, standard 240 deviation and optimum smoothing length. Similarly, spatial smoothing can remove noise. The improvement of the products with the temporal coverage Δt is significant, with the bias decreasing approximately linearly with $\sqrt{\Delta t}$, as illustrated in Fig. 6. Some long-term products were calculated as averages of short-term products, i.e. based on more observations, which would also help reduce the temporal variability and noise of these products compared to short-term products. The bias of all the 165 products are in the range $\sim 0.3 - 40 \text{ m a}^{-1}$, with a standard deviation in the range $\sim 0.4 - 22 \text{ m a}^{-1}$. Smoothing both temporally 245 or spatially reduced the standard deviation. After applying optimum spatial smoothing, the standard deviation is reduced to a range of $\sim 0.4 - 10 \text{ m a}^{-1}$. The optimum smoothing length σ is typically in the order of 500-3000m.

5 Discussion

5.1 Assessment of surface velocity products from space

In the interior regions of the Greenland ice sheet, validation of satellite derived ice velocity and surface elevation products is 250 generally limited due to lack of in-situ data. Our GPS stake network provide a unique dataset for validation in the interior accumulation area of the ice stream, and it represents a range of velocities and velocity gradients over one order of magnitude in the NEGIS ice stream, the shear margins and the surrounding slow moving areas. However, the assessment is restricted due to the limited spatial extent of the GPS data, and our conclusions may not apply to margin areas with very fast flow, seasonal variability or high surface slopes. 255 In our comparison, the DTU-Space-S1 experimental product stands out among all the investigated products with its short temporal coverage ($\sim 10-20$ days), low bias of 0.35 m a^{-1} and the low standard deviation of 0.55 m a^{-1} , which can be reduced



to 0.53 m a^{-1} after optimum smoothing of 354 m. The AWI-TSX experimental product stands out because of its minimum standard deviation of 0.39 m a^{-1} of all the investigated products, and its high spatial resolution, which results in a very low optimum smoothing length of 10 m, i.e. no further smoothing is needed to reduce the noise. The bias of the AWI-TSX product 260 is 0.51 m a^{-1} , and also among the lowest of the investigated products. Both these products are based entirely on InSAR processing methods.

The widely used multi-year velocity product from MEaSURE, MEaSUREs multi-year v1 product (Joughin et al., 2017), has a bias of 0.77 m a^{-1} and a standard deviation of 0.50 m a^{-1} . Since this product is already a 20-year average, the optimum smoothing length is only 200 m and only slightly reduces the standard deviation to 0.48 m a^{-1} . It is notable, that the bias of this product is 265 similar to several other MEaSUREs products with shorter temporal coverage, while the standard deviation of this product is smaller than the other MEaSUREs products. If the interior of the ice sheet changes slowly over time, the differences between the temporal stamp of the GPS observations and of the multi-year velocity product covering 1995-2015 may become important. However, MEaSUREs winter velocity map from 2008-2009, the MEaSUREs InSAR v2 product, performed very similar to 270 the MEaSUREs multi-year v1 product, with a bias of 0.89 m a^{-1} , standard deviation of 0.46 m a^{-1} , and an optimum smoothing length of 51 m. The winter velocity product from 2008-2009 is based on InSAR and stands out with its low standard deviation and a relative short temporal coverage of nine months. The similar agreement between these products and the GPS velocities suggest that the velocity in the interior part of NEGIS has not changed significantly in the last decade.

The five products with a minimum bias are the MEaSUREs ITS_LIVE 6-year average product with a bias of 0.31 m a^{-1} , the MEaSUREs combined SAR&Landsat v1 1-year product for 2015 with a bias of 0.33 m a^{-1} , the DTU-Space-S1 18-day product 275 from 2019 with a bias of 0.35 m a^{-1} , the ESA CCI annual velocity product from 2015-2016 with a bias of 0.43 m a^{-1} , and the 24-days PROMICE product from 2018-02 with a bias of 0.46 m a^{-1} . Of these, the DTU-Space-S1 product stands out with its short temporal coverage, low standard deviation and low optimal smoothing length. MEaSUREs ITS_LIVE product stands 280 out with its long temporal coverage, low standard deviation, very low optimal smoothing length, and because it is the only product in our study entirely based on optical feature tracking. The other products have a time stamp that overlap with the first one to two years of the GPS observation period, but their standard deviations are much higher due to the SAR processing techniques. The MEaSUREs combined SAR&Landsat v1 product has a standard deviation of 1.85 m a^{-1} , which reduces to 1.65 m a^{-1} after optimum smoothing over 1224 m. The ESA CCI product performs very similar with a standard deviation of 1.94 m a^{-1} , which reduces to 1.11 m a^{-1} after optimum smoothing length over 1185 m. The PROMICE product with its very high temporal resolution of 24 days has a standard deviation of 5.39 m a^{-1} , which reduces to 2.6 m a^{-1} after optimum smoothing 285 length over 2264 m.

Among the top five products with lowest standard deviation, three are entirely based on InSAR (DTU-Space-S1 from 2019; AWI-TSX from 2016-2017; MEaSUREs InSAR v2 from 2008-2009), and two are combined products averaged over a multi-year period (MEaSUREs multi-year product v1, 1995-2015; MEaSUREs multi-year SAR&Landsat v1, 2014-2018). Overall, the assessments show that for interior velocity estimates, the InSAR based products stand out with higher resolution in time 290 and space and lower errors. SAR based products (ESA CCI, PROMICE and MEaSUREs) can obtain comparable accuracy and



low standard deviation, if they are averaged over time (multi-year averages) and smoothed spatially. The optical product (MEaSUREs ITS_LIVE) can obtain a comparable high accuracy when averaged over long time intervals (decades), but the standard deviation is slightly higher than the radar based products.

5.2 Estimated errors of satellite derived strain rates

295 Strain rates are derived from the satellite-based products as derivatives of the velocity fields and have therefore higher uncertainties. We calculate the satellite-based strain rate tensor directly from the gridded velocity product without smoothing, and rotate according to the local flow direction in order to determine the strain rates along the flow. Our assessment provides an estimate of the strain rates error depending on the resolution from the standard deviation of the velocity product. For velocity products with a standard deviation in the order of 0.5 m a^{-1} , the strain rate uncertainty is in the order of 10^{-3} a^{-1} on a 500 m grid, 300 but it could be improved by smoothing the velocity product using the optimum smoothing length from the assessment. We compare the GPS derived strain rates with strain rates from MEaSUREs multi-year v1 velocity product in transects across the NEGIS (Fig. 3) and along NEGIS (fig. 4). While the GPS derived strain rates are limited in resolution and do not exactly capture the maximum strain rate at the southern shear margin, they do capture the enhanced strain rates in the shear margins.

5.3 Structure and flow of NEGIS

305 The assessment of satellite-based velocity and height products provides confidence in the satellite-based products in the interior regions of the Greenland ice sheets. Thereby, it enables us to use the GPS derived velocities and strain rates in combination with satellite-based data to characterize spatial patterns in surface structure and ice flow in the interior part of the NEGIS ice stream.

The flow and surface topography across the NEGIS ice stream reveal a distinct 25 km wide fast-flowing ice stream near the 310 EastGRIP site, which is sharply marked at both sides in speed, strain rates and surface geometry (Fig. 3). The cross sections show a central 10 km wide section with an almost uniform speed of 55 m a^{-1} , and well-defined shear margins at both sides with a width of about 5 km separating the ice stream from the surrounding slow-moving ice (Fig. 3). The velocities are above 20 m a^{-1} on the southern side where a broad flow field is merging with NEGIS, and approximately 10 m a^{-1} on the northern side (Fig. 2 and 3). The strain rates are at a level of approximately 10^{-4} a^{-1} within the ice stream and in the surrounding slow 315 moving areas outside the ice stream. In the shear margins, they increase with an order of magnitude to a maximum value of approximately 10^{-3} a^{-1} . The remarkable uniform velocities and low strain rates in the fast flowing central band of NEGIS with narrow shear zones at the margins, support a softening of the ice in the margins due to higher temperatures or ice fabric (Holschuh et al., 2019). The surface topography reveals a 30-40 m deep trough coinciding with the fast flow within NEGIS and with an additional well-defined 10-20 m deep troughs marking the shear margins. These deep shear margin troughs form 320 due to a combination of enhanced longitudinal stretching, transverse compression and shear as the ice flow enters the fast flowing ice stream from both sides with an angle of $\sim 15^\circ$, accelerates and turns, and an enhanced firn densification in the shear margins due to the enhanced horizontal deformation (Riverman et al., 2019a).



The location of the shear margins cannot be clearly linked to the bedrock topography in the area (Christianson et al., 2014; Franke et al., 2020). Christianson et al. (2014) proposed that the shear margins of NEGIS are controlled by a self-stabilizing mechanism related to gradients in the subglacial hydropotential due to the surface troughs that restrict widening of the ice stream, and the internal stratigraphy suggests that the shear margins have been relatively stable during the Holocene (Keisling et al., 2014). Detailed maps of bedrock topography in the area reveal subglacial landforms proposed to be related to basal erosion due to the fast flow (Franke et al., 2020), and elongated bedforms aligned with the flow (Franke et al., 2020; Riverman et al., 2019b). These elongated bedforms are seen in the transects across NEGIS as 100-300 m undulations in bedrock topography (Fig. 3), and they appear here to be related to the location of the shear margins. The southern very well-defined shear margin trough is consistently located above a local bedrock low in the three cross sectional profiles spanning a 5 km distance along NEGIS (Fig. 3). The northern broad shear margin trough is located over a wide bedrock valley, and the shear margin trough narrows from a wide double-trough to a single trough in the three cross sectional profiles over a 5 km distance along NEGIS, as the bedrock valley over the same distance narrows (Fig. 3). Thus, our observations support that these bedforms are related to the shear margins (Franke et al., 2020; Riverman et al., 2019b), but further studies are needed to fully understand the conditions at the shear margins.

The ArcticDEM surface topography of the NEGIS ice stream shows that an organized spatial pattern of wavy undulations develops perpendicular to the NEGIS flow in the area around EastGRIP (Fig. 7). The undulations develop within the fast flowing central flow band of NEGIS in a 25 km section along NEGIS where the surface velocity remain at a level of approximately 55 m a^{-1} . Upstream from this section, the flow accelerates over tens of km with an acceleration of approximately 10 m a^{-1} over 10 km, i.e. longitudinal strain rates of $\sim 10^{-3} \text{ a}^{-1}$. The undulating patterns start forming as ice velocity exceeds a threshold velocity of approximately 55 m a^{-1} , and as the ice flows over a 200-300 m bedrock transition to a bedrock plateau of approximately 200 m elevation and widens (Franke et al., 2020), suggesting that the undulations are related to the bedrock topography (Fig. 4). The undulations in surface slope are connected to undulations in the longitudinal and transverse surface strain rates, and to some degree related to undulations in bedrock topography (Fig. 4). Similar organized undulating patterns in driving stress was previously reported in Antarctic and Greenland ice sheets in fast flowing areas (Sergienko and Hindmarsh, 2013; Sergienko et al., 2014) and related to patterns in basal stress located in areas with significant sliding. These previous studies attributed the patterns to be the result of instabilities related to subglacial water beneath a sliding glacier, and our results support that bedrock topography plays a role in relation to these undulations.

350 5.4 Inferring the upstream flow path from velocity products

Knowing the accurate flowlines of an ice sheet is useful for many applications, such as defining the outlines of drainage basins or to identify the source area for ice flowing through a specific survey site. For studies related to the internal stratigraphy and ice properties, e.g. in ice cores or radar profiles, it is essential to know the upstream flow path in order to infer the deformation history of the internal layers. However, minor uncertainties and bias in satellite-based velocity products can severely affect 355 flow lines traced along the velocity field, as these uncertainties can displace the flowline and propagate along the flow line.



This is particularly critical when the flow is strongly convergent or divergent. To investigate this, we use the whole set of satellite-derived surface velocity products to trace flow lines along NEGIS. We use a starting point at the EastGRIP site, located in the center of our observed area in a relatively narrow section of the NEGIS ice stream. We trace the flow lines upstream into the slower moving areas where flow converges into NEGIS and downstream into faster flow where the ice stream widens. These flow lines differ widely depending on the bias and standard deviation of the products (Fig. 8). We notice that the back-trajectories diverge more than the forward trajectories, and we attribute this to the higher uncertainty of the upstream lower velocities compared to downstream. As a result, it may be better to use surface slopes instead of surface velocity products to trace flow trajectories in slow moving areas.

6 Conclusion

We have presented results from a GPS survey in 2015-2019 of a strain net consisting of 63 stakes near the EastGRIP deep drilling site in the interior northeast Greenland to map surface topography and flow of an interior section of NEGIS in an area near its onset in North Greenland. The GPS derived surface velocities are $>55 \text{ m a}^{-1}$ within an approximately 10 km wide central flow band, and drops abruptly at the shear margins to approximately 10 m a^{-1} and 25 m a^{-1} at the northern and southern sides, respectively. The flow enters NEGIS at an angle of approximately 15° from both sides. Strain rates are in the order of 10^{-3} a^{-1} in the shear margins with enhanced longitudinal stretching, transverse compression and shearing, and an order of magnitude smaller elsewhere. Our results suggest that the location of the shear margins is related to 100-300 m bedrock lows. We compare our GPS derived heights and surface velocities with the ArcticDEM height model (Porter et al., 2018), as well as published and experimental remote sensing velocity products in order to validate and assess these products. We include surface velocity products from the MEaSUREs program, the ESA CCI program, the PROMICE program, and experimental data products from MEaSUREs, DTU-Space and AWI. For each product, we calculate the bias, the standard deviation relative to the GPS derived surface velocities, and the spatial smoothing that minimizes the standard deviation. Our assessments show:

- the ArcticDEM height model is accurate at the strain net poles within 0.48 m with a standard deviation of 0.53 m compared to the GPS positions, without considering the different time stamps of the observations. The uncertainty of the GPS positions is in the order of 10^{-2} m .
- Among the top five surface velocity products with lowest standard deviation compared to the GPS derived surface velocities, three are entirely based on InSAR (DTU-Space, 2019; AWI-TSX, 2016-2017; MEaSUREs winter velocity by InSAR v2, 2008-2009), and two are combined products averaged over a multi-year period (MEaSUREs multi-year product, 1995-2015; MEaSUREs multi-year SAR and Landsat, 2014-2018).
- SAR based surface velocity products from ESA CCI, PROMICE and MEaSUREs can obtain comparable precision compared to the GPS derived surface velocities if they are averaged over longer time periods (years) and smoothed spatially, and they generally obtain a low bias.



- The experimental optical velocity product from MEaSUREs can also obtain a comparable precision as the SAR based products if it is averaged over long periods (several years), but the bias is slightly higher.

Overall, the assessments show that for interior velocity estimates, the InSAR based products stand out with higher resolution
390 in time and space and low errors. For all products, longer observation time improves the products in these interior areas where surface velocity has not changed significantly over the last decade.

We investigate flow along the centerline of NEGIS and find that regular undulating patterns form in surface slope and strain rates when the surface velocity exceeds approximately 55 m a^{-1} , and the formation of these undulations appears to be related to bedrock topography. Finally, we investigated the uncertainties in derived flow trajectories along NEGIS depending on the
395 accuracy and precision of the satellite derived velocity products. We traced flow lines from our observed area, and show that the flow lines differ significantly among the assessed products depending on their bias.

Author contributions: C.S.H. and A.G. designed and carried out the study. H.A.K., P.V., N.B.K. and D.D.J. contributed to the field work. S.A.K. contributed to the design of the GPS survey and the validation of the GPS processing with GIPSY-OASIS
400 software. N.N., A.S., A.K. and J.K.A. provided remote sensing velocity products. C.S.H. and A.G. prepared the draft manuscript, and all authors provided comments and input to the manuscript.

Competing interests: The authors declare that they have no conflict of interest.

405 *Acknowledgments:* This work was supported by a Dancea grant from the Danish Environmental Protection Agency (EPA), by the PROMICE project, by the European Space Agency (ESA) Climate Change Initiative (CCI, CCI+) Greenland ice sheet project (contracts No. 4000112228 and 4000126523), and by research grants from the Villum Foundation (grant No. 2361 and 16572). Logistical support was provided by the East Greenland Ice-Core Project. EastGRIP is directed and organized by the Center of Ice and Climate at the Niels Bohr Institute. It is supported by funding agencies and institutions in Denmark (A. P.
410 Møller Foundation, University of Copenhagen), the USA (U.S. National Science Foundation, Office of Polar Programs), Germany (AlfredWegener Institute, Helmholtz Centre for Polar and Marine Research), Japan (National Institute of Polar Research and Arctic Challenge for Sustainability), Norway (University of Bergen and Bergen Research Foundation), Switzerland (Swiss National Science Foundation), France (French Polar Institute Paul-Emile Victor, Institute for Geosciences and Environmental research), and China (Chinese Academy of Sciences and Beijing Normal University). TerraSAR-X and
415 TanDEM-X data used in the processing of surface velocities were made available through DLR proposals HYD2059 and DEM_GLAC1608. N.N. received funding from the European Union's Horizon 2020 research and innovation programme under grant agreement No. 689443 via project iCUPE (Integrative and Comprehensive Understanding on Polar Environments). The ArcticDEM was provided by the Polar Geospatial Center under NSF-OPP awards 1043681, 1559691, and 1542736. Ice velocity maps were produced as part of the Programme for Monitoring of the Greenland Ice Sheet (PROMICE) using



420 Copernicus Sentinel-1 SAR images distributed by ESA, and were provided by the Geological Survey of Denmark and Greenland (GEUS) at <http://www.promice.dk>

References

Altamimi, Z., P. Rebischung, L. Metivier, and X. Collilieux: ITRF2014: A new release of the International Terrestrial Reference Frame modeling nonlinear station motions, *J. Geophys. Res. Solid Earth*, 121, doi:10.1002/2016JB013098, 2016.

425 Bevis, M., J. Wah, S. A. Khan, F. B. Madsen, A. Brown, M. Willi, E. Kendrick, P. Knudsen, J. E. Box, T. van Dam, D. J. Caccamise II, B. Johns, T. Nylen, R. Abbott, S. White, J. Miner, R. Forsberg, H. Zhou, J. Wang, T. Wilson, D. Bromwiche, and O. Francis: Bedrock displacements in Greenland manifest ice mass variations, climate cycles and climate change. *PNAS*, doi:10.1073/pnas.1204664109, 2019.

Boehm J., B. Werl, H. Schuh: Troposphere mapping functions for GPS and very long baseline interferometry from European

430 Centre for medium-range weather forecasts operational analysis data. *J. Geophys. Res.* 111, B02406, 2006.

Choi, Y., Morlighem, M., Rignot, E., Mouginot, J., & Wood, M.: Modeling the response of Nioghalvfjerdsfjorden and Zachariae Isstrøm glaciers, Greenland, to ocean forcing over the next century. *Geophysical Research Letters*, 44, 11,071–11,079, doi.org/10.1002/2017GL075174, 2017.

Christianson, K., L. E. Peters, R. B. Alley, A. Anandakrishnan, R. W. Jacobel, K. L. Riverman, A. Muto and B. A. Keisling:

435 Dilatant till facilitates ice-stream flow in northeast Greenland. *Earth and Planetary Science Letters*, 401, 57-69, <https://doi.org/10.1016/j.epsl.2014.05.060>, 2014.

Dall, J., Kusk, A., Nielsen, U., Merryman Boncori, J.P.: Ice Velocity Mapping Using TOPS SAR Data and Offset Tracking. In: Proceedings of 9th International Workshop Fringe 2015. ESA Publication SP-731. <https://doi:10.5270/Fringe2015.91>, 2015.

ESA Greenland Ice Sheet CCI project team. *ESA Greenland Ice Sheet Climate Change Initiative (Greenland_Ice_Sheet_cci)*:

440 Greenland Ice Velocity Map, Winter 2015-2016, v1.2. Centre for Environmental Data Analysis, 2020-02-18. <https://catalogue.ceda.ac.uk/uuid/302f379334e84664bd3409d08eca6565>, 2018.

Franke, S., Jansen, D., Binder, T., Dörr, N., Helm, V., Paden, J., Steinhage, D. and Eisen O.: Bed topography and subglacial landforms in the onset region of the Northeast Greenland Ice Stream. *Annals of Glaciology*, 1–11. <https://doi.org/10.1017/aog.2020.12>, 2020.

445 Gardner, A. S., G. Moholdt, T. Scambos, M. Fahnestock, S. Ligtenberg, M. van den Broeke, and J. Nilsson: Increased West Antarctic and unchanged East Antarctic ice discharge over the last 7 years, *Cryosphere*, 12(2): 521–547, doi:10.5194/tc-12-521-2018, 2018.

Gardner, A. S., M. A. Fahnestock, and T. A. Scambos: *ITS_LIVE Regional Glacier and Ice Sheet Surface Velocities*. Data archived at National Snow and Ice Data Center; doi:10.5067/6II6VW8LLWJ7, 2019 [2019-05-01].



450 Gillet-Chaulet, F., G. Durand, O. Gagliardini, C. Mosbeux, J. Mouginot, F. Rémy, and C. Ritz: Assimilation of surface velocities acquired between 1996 and 2010 to constrain the form of the basal friction law under Pine Island Glacier, *Geophys. Res. Lett.*, 43, 10,311–10,321, doi:10.1002/2016GL069937, 2016.

Holschuh, N., Lilien, D. A., and Christianson, K.: Thermal weakening, convergent flow, and vertical heat transport in the Northeast Greenland Ice Stream shear margins. *Geophysical Research Letters*, 46, 8184–8193.

455 <https://doi.org/10.1029/2019GL083436>, 2019.

Hvidberg, C. S., K. Keller, N. S. Gundestrup, C. C. Tscherning and R. Forsberg: Mass balance and surface movement of the Greenland Ice Sheet at Summit, Central Greenland. *Geophys. Res. Letters*, 24(18), 2307-2310, <https://doi.org/10.1029/97GL02280>, 1997.

Hvidberg, C. S., K. Keller, and N. S. Gundestrup: Mass balance and ice flow along the north-northwest ridge of the Greenland ice sheet at NorthGRIP. *Annals of Glaciology*, 35, 521-526, <https://doi.org/10.3189/172756402781816500>, 2002.

Ibáñez D., Rovira-García A., Sanz J., Juan JM., Gonzalez-Casado G., Jimenez-Baños D., López-Echarzarreta C., Lapin I. The GNSS Laboratory Tool Suite (gLAB) updates: SBAS, DGNSS and Global Monitoring System. 9th ESA Workshop on Satellite Navigation Technologies (NAVITEC 2018), Noordwijk, The Netherlands. December 5 - 7, 2018. DOI: 10.1109/NAVITEC.2018.8642707, 2018.

460 IMBIE Team: Mass balance of the Greenland Ice Sheet from 1992 to 2018. *Nature*, <https://doi.org/10.1038/s41586-019-1855-2>, 2019.

IPCC: IPCC Special Report on the Ocean and Cryosphere in a Changing Climate. H.-O. Pörtner, D.C. Roberts, V. Masson-Delmotte, P. Zhai, M. Tignor, E. Poloczanska, K. Mintenbeck, A. Alegría, M. Nicolai, A. Okem, J. Petzold, B. Rama, N.M. Weyer (eds.). In press, 2019.

470 Joughin, I.R., R. Kwok and M.A. Fahnestock: Interferometric estimation of three-dimensional ice-flow using ascending and descending passes. *IEEE Trans. Geosci. Remote Sens.*, 36(1), 25–37, doi: 10.1109/36.655315, 1998.

Joughin, I.: Ice-sheet velocity mapping: a combined interferometric and speckle-tracking approach. *Annals of Glaciology*, 34, 195-201, 2002.

Joughin, I., Smith, B. E., Howat, I. M., Scambos, T., and Moon, T.: Greenland flow variability from ice-sheet-wide velocity mapping. *J. Glaciol.*, 56, 415–430, 2010.

475 Joughin, I., B. Smith, I. Howat, and T. Scambos: MEaSUREs Multi-year Greenland Ice Sheet Velocity Mosaic, Version 1. NASA National Snow and Ice Data Center Distributed Active Archive Center, Boulder, Colorado USA. doi: <https://doi.org/10.5067/QUA5Q9SVMSJG>. 2016.

Joughin, I., B. E. Smith, and I. M. Howat: A complete map of Greenland ice velocity derived from satellite data collected over 480 20 years. *Journal of Glaciology*, doi: 10.1017/jog.2017.73, 2017.

Joughin, I., Smith, B. E., and Howat, I.: Greenland Ice Mapping Project: ice flow velocity variation at sub-monthly to decadal timescales, *The Cryosphere*, 12, 2211–2227, <https://doi.org/10.5194/tc-12-2211-2018>, 2018.



Karlsson, N. B. and D. Dahl-Jensen: Response of the large-scale subglacial drainage system of Northeast Greenland to surface elevation changes. *The Cryosphere*, 9, 1465–1479, doi:10.5194/tc-9-1465-2015, 2015.

485 Keisling, B. A., K. Christianson, R. B. Alley, L. E. Peters, J. E. M. Christian, S. Anandakrishnan, K. L. Riverman, A. Muto and R. W. Jacobel: Basal conditions and ice dynamics inferred from radar-derived internal stratigraphy of the northeast Greenland ice stream. *Annals of Glaciology*, 55(67), 127–137, doi:10.3189/2014AoG67A090, 2014.

Khan, S. A., Kjaer, K. H., Bevis, M., Bamber, J. L., Wahr, J., Kjeldsen, K. K., Bjork, A. A., Korsgaard, N. J., Stearns, L. A., van den Broeke, M. R., Liu, L., Larsen, N. K., and Muresan, I. S.: Sustained mass loss of the northeast Greenland ice sheet triggered by regional warming. *Nature Climate Change*, 4(4), 292–299, doi: 10.1038/NCLIMATE2161, 2014.

490 Khan, S. A., A. Aschwanden, A. A. Bjørk, J. Wahr, K. K. Kjeldsen, and K. H. Kjær: Greenland ice sheet mass balance: a review. *Rep. Prog. Phys.* 78, doi:10.1088/0034-4885/78/4/046801, 2015.

Kouba, J.: Implementation and testing of the gridded Vienna Mapping Function 1 (VMF1). *J. Geophys. Res.* 82, 193–205, 2007.

495 Kusk, A., Boncori, J.P.M., Dall, J.: An automated system for ice velocity measurement from SAR. *Proceedings of the 12th European Conference on Synthetic Aperture Radar (EUSAR 2018)*, 929–932, 2018.

Mankoff, K. D., W. Colgan, A. Solgaard, N. B. Karlsson, A. P. Ahlstrøm, D. van As, J. E. Box, S. A. Khan, K. K. Kjeldsen, J. Mouginot, and R. S. Fausto: Greenland Ice Sheet solid ice discharge from 1986 through 2017. *Earth Syst. Sci. Data*, 11, 769–786, https://doi.org/10.5194/essd-11-769-2019, 2019.

500 Minchew, B. M., C. R. Meyer, A. A. Robel, G. H. Gudmundsson, and M. Simons: Processes controlling the downstream evolution of ice rheology in glacier shear margins: case study on Rutford Ice Stream, West Antarctica. *Journal of Glaciology* (2018), 64(246) 583–594 doi: 10.1017/jog.2018.47, 2018.

Minchew, B. M., C. R. Meyer, S. S. Pegler, B. P. Lipovsky, A. W. Rempel, G. H. Gudmundsson, N. R. Iverson: Comment on ‘Friction at the bed does not control fast glacier flow’. 2019. *Science*, 363, doi: 10.1126/science.aau6055, 2019.

505 Morlighem M. M., C. N. Williams, E. Rignot, L. An, J. E. Arndt, J. L. Bamber, G. Catania, N. Chauché, J. A. Dowdeswell, B. Dorschel, I. Fenty, K. Hogan, I. Howat, A. Hubbard, M. Jakobsson, T. M. Jordan, K. K. Kjeldsen, R. Millan, L. Mayer, J. Mouginot, B. P. Y. Noël, C. O’Cofaigh, S. Palmer, S. Rysgaard, H. Seroussi, M. J. Siegert, P. Slabon, F. Straneo, M. R. van den Broeke, W. Weinrebe, M. Wood, and K. B. Zinglersen: BedMachine v3: Complete bed topography and ocean bathymetry mapping of Greenland from multi-beam echo sounding combined with mass conservation, *Geophys. Res. Lett.*, 44, 510 doi:10.1002/2017GL074954, 2017a.

Morlighem, M. et al.: IceBridge BedMachine Greenland, Version 3. NASA National Snow and Ice Data Center Distributed Active Archive Center, Boulder, Colorado USA. doi: https://doi.org/10.5067/2CIX82HUV88Y. 2017b.

Mouginot J., E. Rignot, B. Scheuchl, I. Fenty, A. Khazendar, M. Morlighem, A. Buzzi, and J. Paden: Fast retreat of Zachariae Isstrøm, northeast Greenland. *Science* 350:1357–1361, doi: 10.1126/science.aac7111, 2015.

515 Mouginot J., Bjørk A. A., Millan R., Scheuchl B., and Rignot E.: Insights on the surge behavior of Storstrømmen and L. Bistrup Brae, Northeast Greenland, over the last century. *Geophys Res Lett* 45:11197–11205, 2018.



Mouginot, J., E. Rignot, A. A. Bjørk, M. van den Broeke, R. Millan, M. Morlighem, B. Noël, B. Scheuchl, and M. Wood: Forty-six years of Greenland Ice Sheet mass balance from 1972 to 2018. *Proceedings of the National Academy of Sciences* May 2019, 116 (19) 9239-9244; DOI: 10.1073/pnas.1904242116, 2019.

520 Nagler, T., H. Rott, M. Hetzenecker, J. Wuite, and P. Potin: The Sentinel-1 Mission: New Opportunities for Ice Sheet Observations. *Remote Sensing*, 7, 9371-9389, doi:10.3390/rs70709371, 2015.

Noh, M.-J., and I. M. Howat. 2015. Automated stereo-photogrammetric DEM generation at high latitudes: Surface extraction with TIN-based search-space minimization (SETSM) validation and demonstration over glaciated regions. *GIScience & Remote Sensing* 52 (2):198–217. doi:10.1080/15481603.2015.1008621.

525 Porter, C., Morin, P., Howat, I., Noh, M.-J., Bates, B., Peterman, K., Keesey, S., Schlenk, M., Gardiner, J., Tomko, K., Willis, M., Kelleher, C., Cloutier, M., Husby, E., Foga, S., Nakamura, H., Platson, M., Wethington, M. Jr., Williamson, C., Bauer, G., Enos, J., Arnold, G., Kramer, W., Becker, P., Doshi, A., D’Souza, C., Cummens, P., Laurier, F., Bojesen, M.: ArcticDEM. <https://doi.org/10.7910/DVN/OHHUKH>, Harvard Dataverse, V1, 2018 [Date Accessed 2017-06-07].

Riverman, K. L., Alley, R. B., Anandakrishnan, S., Christianson, K., Holschuh, N. D., Medley, B., Muto, A., and Peters, L.

530 E.: Enhanced firn densification in high-accumulation shear margins of the NE Greenland Ice Stream. *Journal of Geophysical Research: Earth Surface*, 124, 365–382. <https://doi.org/10.1029/2017JF004604>, 2019a.

Riverman, K. L., S. Anandakrishnan, R. B. Alley, N. Holschuh, C. F. Dow, A. Muto, B. R. Parizek, K. Christianson, and L.

E. Peters: Wet subglacial bedforms of the NE Greenland Ice Stream shear margins. *Annals of Glaciology* 60(80), 91–99. <https://doi.org/10.1017/aog.2019.43>, 2019b.

535 Sanz Subirana, J., Juan Zornoza, J. M., & Hernández-Pajares, M.: GNSS Data Processing Book, Vol. I: Fundamentals and Algorithms. TM-23/1. Noordwijk: ESA Communications, 2013.

Scherneck, H. G., and M. S. Bos: Ocean tide and atmospheric loading. In: IVS 2002 General Meeting Proceedings, Tsukuba, Japan, February 4-7, 2002.

Sergienko, O. V., and R. C. A. Hindmarsh: Regular patterns in frictional resistance of ice-stream beds seen by surface data

540 inversion. *Science*, 342(6162), 1086–1089, doi:10.1126/science.1243903, 2013.

Sergienko, O. V., T. T. Creyts, and R. C. A. Hindmarsh: Similarity of organized patterns in driving and basal stresses of Antarctic and Greenland ice sheets beneath extensive areas of basal sliding. *Geophys. Res. Lett.*, 41, doi:10.1002/2014GL059976, 2014.

Solgaard, A., and A. Kusk: Programme for monitoring of the Greenland ice sheet (PROMICE): Greenland ice velocity.

545 Geological survey of Denmark and Greenland (GEUS), doi:

<https://doi.org/10.22008/PROMICE/DATA/SENTINEL1ICEVELOCITY/GREENLANDICESHEET/V1.0.0>, 2019.

Stearns, L. A. and C. van der Veen: Friction at the bed does not control fast glacier flow. *Science* 361, 273–277 (2018), doi: 10.1126/science.aat2217, 2018.

Strozzi, T., A. Luckman, T. Murray, U. Wegmüller, and C. L. Werner: Glacier motion estimation using SAR offset-tracking

550 procedures, *IEEE Trans. Geosci. Remote Sens.*, 40(11), 2384–2391, 2002.



Vallelonga, P., K. Christianson, R. B. Alley, S. Anandakrishnan, J. E. M. Christian, D. Dahl-Jensen, V. Gkinis, C. Holme, R. W. Jacobel, N. B. Karlsson, B. A. Keisling, S. Kipfstuhl, H. A. Kjær, M. E. L. Kristensen, A. Muto, L. E. Peters, T. Popp, K. L. Riverman, A. M. Svensson, C. Tibuleac, B. M. Vinther, Y. Weng, and M. Winstrup: Initial results from geophysical surveys and shallow coring of the Northeast Greenland Ice Stream (NEGIS). *The Cryosphere*, 8, 1275–1287, doi:10.5194/tc-8-1275-2014, 2014.

Werner, C., U. Wegmüller, T. Strozzi, and A. Wiesmann: Processing strategies for phase unwrapping for INSAR applications, paper presented at European Conference on Synthetic Aperture Radar: EUSAR2002, Verband der Elektrotech. Elektron. Informationstechnik, Cologne, Germany, 4–6 June, 2002.

560



Comparison of results	Stake No.	ΔNE (m)	ΔH (m)
GPS (gLAB vs. GIPSY-OASIS)	Rx85 2018	0.0037	0.0039
	Rx85 2019	0.0165	0.0143
GPS (gLAB vs. CSRS-PPP)	Rx85 2018	0.0060	0.0121
	Rx85 2019	0.0018	0.0176
GPS (GIPSY-OASIS vs. CSRS-PPP)	Rx85 2018	0.0026	0.0082
	Rx85 2019	0.0167	0.0032

Table 1. Assesment of the GPS positions for two stake observations in 2018 and 2019. Top lines: assessment of the processing results, gLAB vs. GIPSY-OASIS. The processing results from the open source Canadian service CSRS-PPP software v. 1.05 is shown for comparison. ΔNE is the difference in horizontal positions, and ΔH is the difference in vertical positions.

Product	t_start	t_end	Δt (a)	bias (m)	RMS (m)	σ (m)	δ (m)
AWI-TSX	2016-09-07	2018-01-03	1.2923	0.512756	0.388398	10.01	30
MEaSUREs InSAR v2	2008-09-15	2009-06-16	0.7502	0.890984	0.458783	51.07	500
MEaSUREs Multi-year v1	1995-01-12	2015-10-31	20.7995	0.767592	0.495511	202.48	250
DTU-Space-S1	2019-01-01	2019-01-18	0.0465	0.352026	0.548307	353.97	50
MEaSUREs SAR&Landsat v1	2014-12-01	2018-11-30	3.9973	0.553502	0.697714	379.91	500
ENVEO ESA CCI	2014-10-01	2019-04-12	4.5284	1.282672	0.713517	593.75	250
PROMICE	2016-09-14	2019-06-17	2.7543	1.000318	0.738214	448.83	500
MEaSUREs ITS_LIVE	2013-01-01	2018-01-01	5.9959	0.306062	0.866842	27.34	240
MEaSUREs ITS_LIVE	1985-01-01	2020-04-01	35.2471	0.467395	0.880819	380.93	120
MEaSUREs ITS_LIVE	2018-01-01	2018-12-31	0.9966	0.645198	0.954738	50.90	240

Table 2. The table shows the assessment results for the ten velocity products with the smallest standard deviation (RMS). The products are sorted with increasing RMS. Notice that the AWI-TSX, the DTU-Space-S1, and the MEaSUREs ITS_LIVE products are also among the ten products with the smallest bias. The complete list of assessment results can be found in Supplementary Table S2.

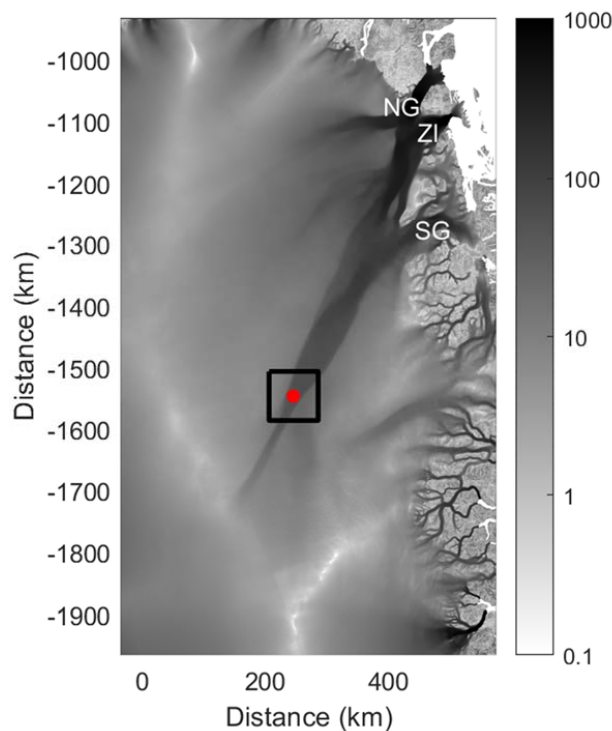


Figure 1. Map of the surface velocity in NE Greenland in m a^{-1} from MEaSUREs multi-year Greenland Ice Sheet velocity v1 product, 1995–2015 (Joughin et al., 2016, 2017), showing the NEGIS ice stream and its three main outlets, Nioghalvfjerdsfjorden glacier (NG), Zachariae Isstrom (ZI), and Storstrømmen Glacier (SG). The box shows the outline of the map in Fig. 2, and the red dot indicates the EastGRIP site ($75^{\circ}38'N, 35^{\circ}60'W$).

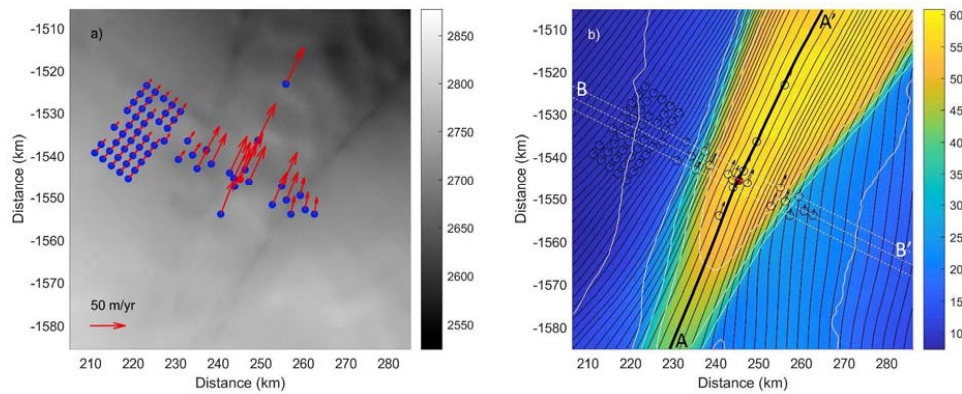


Figure 2. Maps of a 80 km x 80 km area around the EastGRIP site showing the GPS stake network (blue dots/circles), the central reference stake at the EastGRIP site (red dot), and the GPS derived surface velocities (red/black arrows) on an underlying map of: a) detailed surface elevation map (in meters) from ArcticDEM (Porter et al., 2018)) with a velocity scale bar, and b) MEaSUREs multi-year Greenland Ice Sheet Velocity v1 product (in m a^{-1}) (Joughin et al., 2016, 2017) with velocity contours and flow lines. The central flow line through EastGRIP is marked (black line). Ice flow and surface elevations along the central flow line A A' (black) and the three transverse lines B B' (white) are shown in Figs. 3 and 4, respectively.

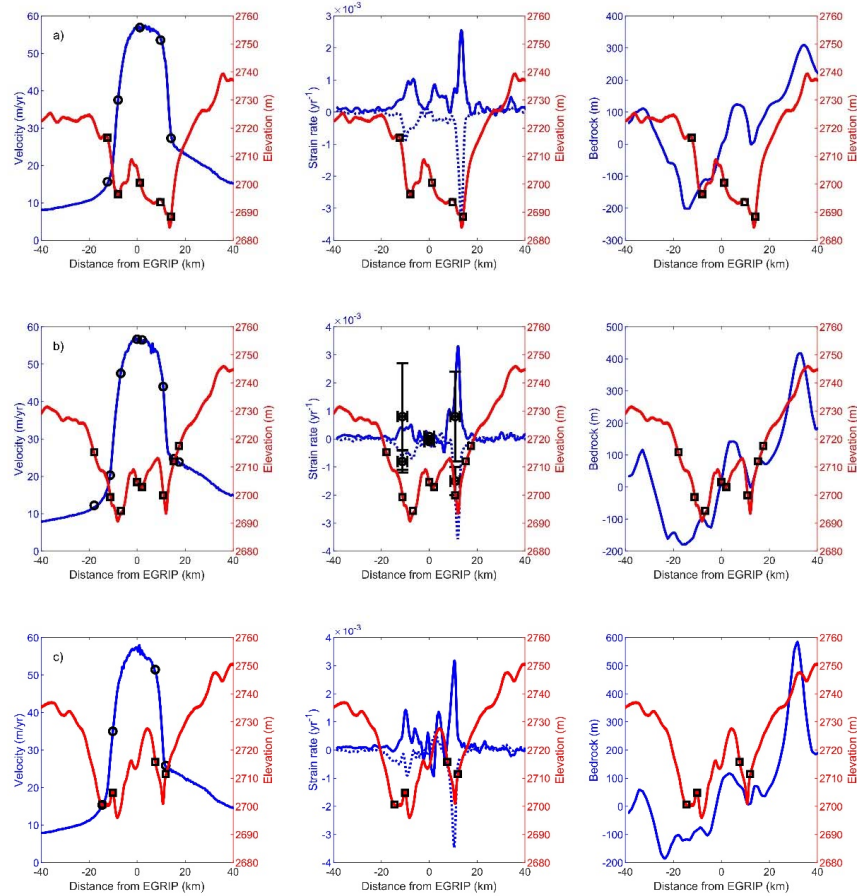


Figure 3. Ice flow and surface elevations of three cross sections of NEGIS separated by 2.5 km: a) downstream from the EastGRIP site, b) at the EastGRIP site, and c) upstream from the EastGRIP site (the cross sections are indicated on Fig. 2b). For each cross section, the three plots are: Left: Surface velocity (blue) and surface elevation (red). Middle: surface strain rates, longitudinal and transverse relative to the local flow direction (blue full/dotted) and surface elevation (red). Right: Surface elevation (red) and bedrock topography (blue). GPS observations are shown as black circles/squares at three stakes marked in Fig. 5. Surface elevation is from the ArcticDEM (Porter et al., 2018), surface velocity and strain rate profiles are derived from MEASUREs multi-year Greenland Ice sheet velocity v1 product (Joughin et al., 2016, 2017), and the bedrock topography is from BedMachine v3 (Morlighem et al., 2017a, 2017b).

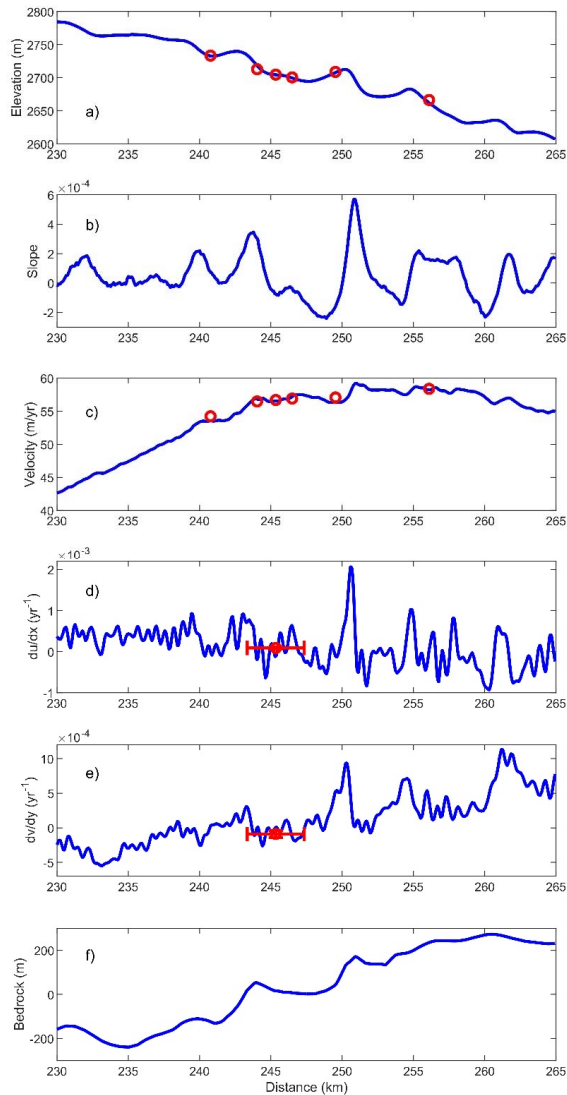


Figure 4. Variations along the central flowline of a) Surface elevation, b) surface slope, c) surface velocity, d) longitudinal strain rate $\dot{\epsilon}_{x'} = \partial u'/\partial x'$, e) transverse strain rate $\dot{\epsilon}_{y'} = \partial v'/\partial y'$, where prime indicates coordinates along and transverse to the flowline, and f) bedrock topography. The profiles in blue are derived from the ArcticDEM (Porter et al., 2018), MEaSUREs multi-year Greenland Ice Sheet Velocity v1 product (Joughin et al., 2016, 2017), and BedMachine v3 (Morlighem et al., 2017a, 2017b). GPS derived surface elevations, velocities and strain rates are shown in red.

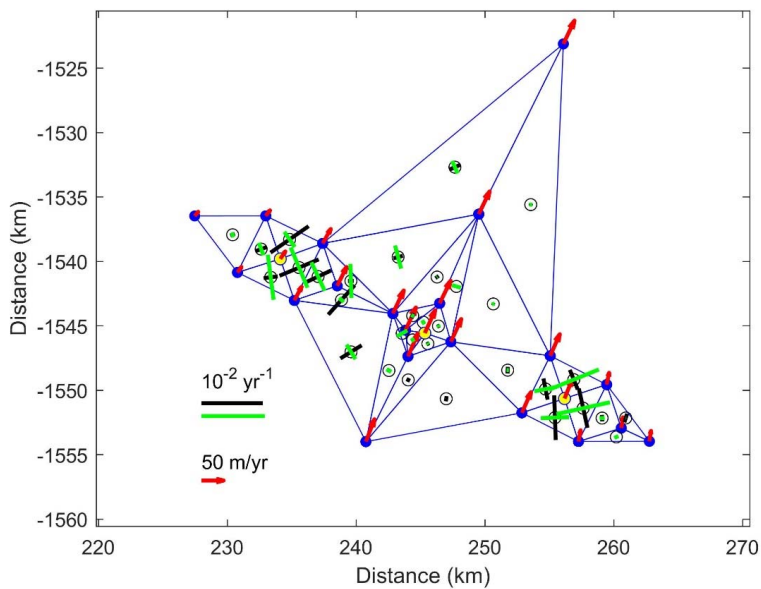


Figure 5. Horizontal principal strain rates for 32 different triangular sections within the GPS array. The principal strain rates are plotted at the centroids of each triangle (black circles) with black lines indicating positive strain rates (extension) and green lines indicating negative strain rates (compression). The GPS-derived surface velocities (red arrows) are plotted at the stakes (blue dots). At three GPS stakes, strain rates along the direction of the flow are calculated, see Fig. 3 (yellow dots).

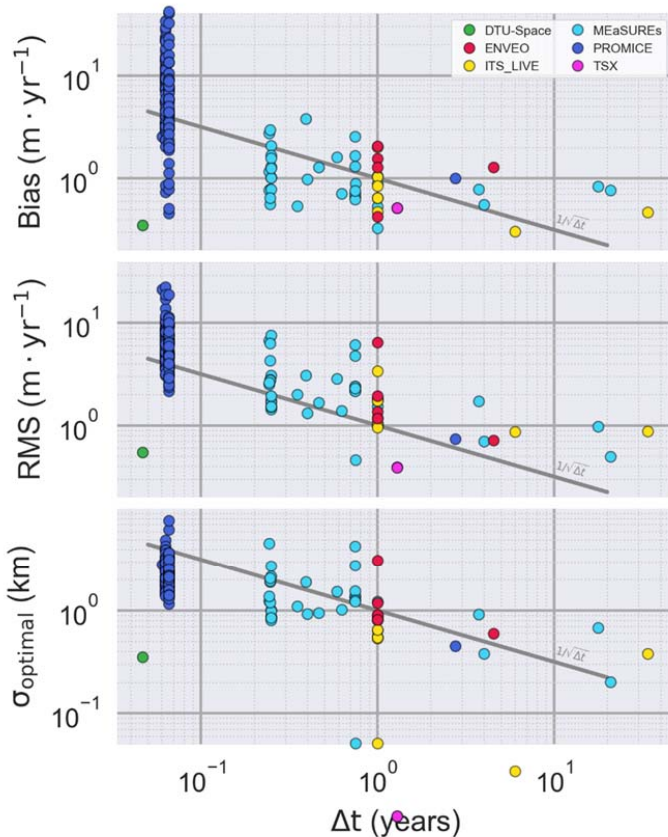


Figure 6. Results of the assessment of a list of 165 satellite-derived surface velocity products. All results are shown as a function of Δt , the timespan of the velocity product. The top panel shows the mean bias of the velocity product compared to the GPS derived velocities at the location of the GPS poles, the middle panel shows the standard deviation of the velocity products relative to GPS derived velocities (RMS), and the bottom panel shows the optimal smoothing length of the velocity product that minimizes the standard deviation (σ). Notice that some products have been averaged over time to provide results with longer temporal coverage. The gray lines suggest a linear dependency of the bias, RMS and σ on temporal coverage Δt .

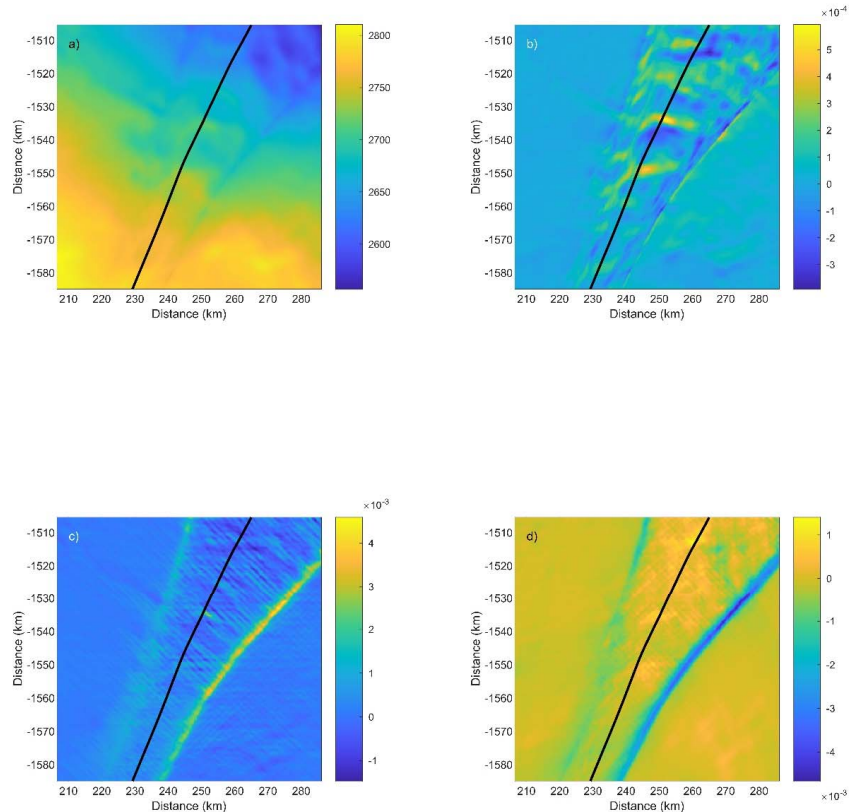


Figure 7. Maps of the 80 km x 80 km section from Fig. 2 with the central flow line marked: a) surface elevation in meters, b) surface slope (dimensionless), both derived from the ArcticDEM (Porter et al., 2018), c) longitudinal strain rate $\dot{\epsilon}_x$, in a^{-1} along the direction of the flow, and d) transverse strain rate $\dot{\epsilon}_y$, in a^{-1} along the transverse direction to the flow, both from MEaSUREs multi-year Greenland Ice Sheet Velocity v1 product (Joughin et al., 2016, 2017).

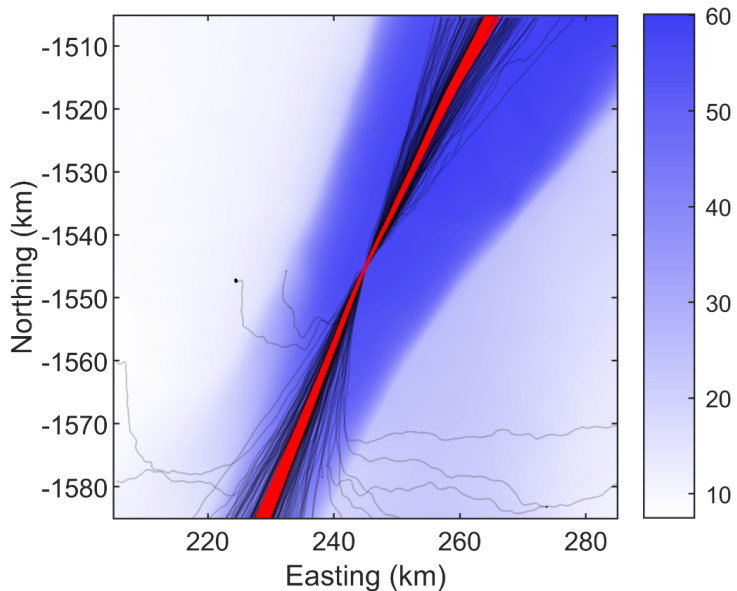


Figure 8. Flowlines through the EastGRIP site (center of plot) calculated from the satellite derived velocity products. The line thickness depends on the bias of the product, with thick lines having a small bias and vice versa. The top four products with smallest bias are marked with red.